

NANO EXPRESS

Open Access



In Situ Synthesis of All-Solid-State Z-Scheme BiOBr_{0.3}I_{0.7}/Ag/AgI Photocatalysts with Enhanced Photocatalytic Activity Under Visible Light Irradiation

Junlin Lu¹, Chaoqun Shang¹, Qingguo Meng², Haiqin Lv², Zhihong Chen^{2,3*} , Hua Liao⁴, Ming Li⁴, Yongguang Zhang³, Mingliang Jin^{1,3}, Mingzhe Yuan², Xin Wang^{1,3*} and Guofu Zhou^{1,3}

Abstract

A series of novel visible light driven all-solid-state Z-scheme BiOBr_{0.3}I_{0.7}/Ag/AgI photocatalysts were synthesized by facile in situ precipitation and photo-reduction methods. Under visible light irradiation, the BiOBr_{0.3}I_{0.7}/Ag/AgI samples exhibited enhanced photocatalytic activity compared to BiOBr_{0.3}I_{0.7} and AgI in the degradation of methyl orange (MO). The optimal ratio of added elemental Ag was 15%, which degraded 89% of MO within 20 min. The enhanced photocatalytic activity of BiOBr_{0.3}I_{0.7}/Ag/AgI can be ascribed to the efficient separation of photo-generated electron-hole pairs through a Z-scheme charge-carrier migration pathway, in which Ag nanoparticles act as electron mediators. The mechanism study indicated that ·O₂⁻ and h⁺ are active radicals for photocatalytic degradation and that a small amount of ·OH also participates in the photocatalytic degradation process.

Keywords: Z-scheme, Photocatalytic, BiOBr_{0.3}I_{0.7}/Ag/AgI

Background

To face critical energy and environmental crises, photocatalysis provides a potential strategy to solve these problems because it not only directly converts solar energy into chemical energy [1–6] but also degrades organic pollutants under solar light irradiation [7–12]. BiOBr_xI_{1-x} solid solution, a novel BiOX-based photocatalyst, has drawn increasing interest because of its unique layered structure with special electrical and catalytic properties as well as its tunable band structure. However, BiOBr_xI_{1-x} has a positive conduction band potential, which makes it exhibit a weak redox capability and restricts it from further application [13, 14].

Recently, it has been proved that Z-scheme photocatalytic systems are able to efficiently enhance the photocatalytic activity of semiconductors due to their special

charge-carrier migration pathway [15–17]. In a typical Z-scheme photocatalytic system, the photo-generated hole and electron with approximate potential in different semiconductors will combine through an electron mediator. Thus, the photo-generated hole with more positive potential and the photo-generated electron with more negative potential can be maintained, which provides better redox ability. At the beginning, the electron mediator in Z-scheme systems was a shuttle redox mediator, such as I⁻/IO₃⁻ and Fe²⁺/Fe³⁺ [15]; this kind of system is called PS-A/D-PS system. However, this kind of electron mediator is unstable for long-term use, and it has low electron transfer efficiency. In order to overcome this shortcoming, an all-solid-state Z-scheme system with noble metal as the electron mediator was developed [18–24]. With noble metal as the electron mediator, the charge transfer and the separation of photo-generated electron-hole pairs are more efficient, showing higher potential in practical applications. More recently, silver iodide has been widely applied in the construction of Z-scheme photocatalytic systems as the reductant due to its particular photolysis characteristics and negative

* Correspondence: chenzhihong1227@sina.com; wangxin@scnu.edu.cn

²Shenyang Institute of Automation, Chinese Academy of Sciences, Guangzhou 511458, China

¹South China Academy of Advanced Optoelectronics, South China Normal University, Guangzhou, Guangdong, Province, China

Full list of author information is available at the end of the article

conduction band potential. The in situ precipitation method provides a facile route for synthesizing silver iodide on the substrate content I element. Furthermore, Ag nanoparticles could be in situ photo-reduced by AgI to construct a Z-scheme photocatalytic system such as $\text{Ag}_3\text{PO}_4/\text{AgI}$ [21], $\text{AgI}/\text{Ag}/\text{AgBr}$ [22], $\text{AgI}/\text{Ag}/\text{Bi}_2\text{MoO}_6$ [23], or $\text{AgI}/\text{Ag}/\text{I}-(\text{BiO})_2\text{CO}_3$ [24]. Thus, using an in situ precipitation and photo-reduction method to construct a novel Z-scheme photocatalyst between $\text{BiOBr}_{0.3}\text{I}_{1-x}$ and AgI would be a possible strategy to enhance the photocatalytic activity and the redox capability of $\text{BiOBr}_{0.3}\text{I}_{1-x}$.

In this study, all-solid-state Z-scheme $\text{BiOBr}_{0.3}\text{I}_{0.7}/\text{Ag}/\text{AgI}$ photocatalysts with different mole ratios of elemental Ag are synthesized via in situ precipitation and photo-reduction methods. The $\text{BiOBr}_{0.3}\text{I}_{0.7}/\text{Ag}/\text{AgI}$ photocatalysts are characterized by various technologies. The photocatalytic activities are evaluated by the degradation of methyl orange (MO) under visible light irradiation, and the optimal molar fraction of elemental Ag in the photocatalyst is determined. In addition, the photocatalytic mechanism is also investigated.

Methods/Experimental

Materials

Bismuth nitrate pentahydrate ($\text{Bi}(\text{NO}_3)_3 \cdot 5\text{H}_2\text{O}$), tertiary butanol (t-BuOH), and silver nitrate (AgNO_3) were purchased from Aladdin Industrial Corporation. Potassium bromide (KBr), potassium iodide (KI), and methyl orange (MO) were purchased from Tianjin Zhiyuan Chemical Co., Ltd. All reagents were used without further purification.

Synthesis of $\text{BiOBr}_{0.3}\text{I}_{0.7}$, $\text{BiOBr}_{0.3}\text{I}_{0.7}/\text{AgI}$, and $\text{BiOBr}_{0.3}\text{I}_{0.7}/\text{Ag}/\text{AgI}$

$\text{BiOBr}_{0.3}\text{I}_{0.7}$ solid solution was prepared by the ultrasound-assisted hydrolysis method according to a previous report [13]. $\text{BiOBr}_{0.3}\text{I}_{0.7}/\text{AgI}$ photocatalyst was synthesized by the in situ precipitation method. A total of 0.5 g of $\text{BiOBr}_{0.3}\text{I}_{0.7}$ was added to 50 ml of appropriate concentration of AgNO_3 solution, where the molar ratio of Ag to I was 15%. Then, the suspension was stirred at room temperature for 1 h to precipitate AgI, and the obtained sample was centrifuged, washed three times with deionized water, and dried at 60 °C for 12 h.

A series of $\text{BiOBr}_{0.3}\text{I}_{0.7}/\text{Ag}/\text{AgI}$ photocatalysts were obtained by in situ precipitation and photo-reduction methods. In a typical experiment, 0.5 g of $\text{BiOBr}_{0.3}\text{I}_{0.7}$ was added to 50 ml of different concentrations of AgNO_3 solutions, and the suspensions were stirred at room temperature for 1 h to precipitate AgI. Next, the obtained suspensions were irradiated with a 300 W Xe lamp ($200 \text{ mW}/\text{cm}^2$) for 10 min with continuous stirring to photo-reduce Ag nanoparticles. Finally, the obtained samples were centrifuged, washed three times with

deionized water and dried at 60 °C for 12 h. By changing the AgNO_3 concentration, $\text{BiOBr}_{0.3}\text{I}_{0.7}/\text{Ag}/\text{AgI}$ with different Ag/I molar ratios was prepared. When the Ag/I molar ratios were 5%, 10%, 15%, and 20%, the as-prepared samples were named BAA-1, BAA-2, BAA-3, and BAA-4, respectively.

Material Characterization

The crystal structures of the prepared photocatalysts were characterized on a Bruker D8 ADVANCE X-ray diffraction (XRD) instrument. Scanning electron microscopy (SEM) images and energy-dispersive spectroscopy (EDS) data were recorded on a Zeiss Ultra 55 thermal FESEM system. Transmission electron microscopy (TEM) and high-resolution TEM (HRTEM) images were recorded on a JEM-2100 instrument. X-ray photoelectron spectroscopy (XPS) measurements were carried out on a Thermo ESCALAB 250Xi instrument with a monochromatized Al K α line source (150 W). Electron paramagnetic resonance (EPR) measurements were carried out on a Bruker ER 200-SRC spectrometer. UV-visible diffuse reflectance spectroscopy (UV-Vis DRS) measurements were conducted on a U-41000 HITACHI spectrophotometer (Tokyo, Japan) using BaSO_4 as the reference.

Photocatalytic Activity Tests

The photocatalytic activity of the prepared photocatalyst was determined by the degradation of MO under visible-light irradiation. In a typical experiment, a 300-W Xe lamp (AM 1.5, output light current of 15 A, $200 \text{ mW}/\text{cm}^2$) with a 400-nm cut-off filter was used as the visible-light source, and the overall system was cooled by circulating water. A total of 100 mg of the prepared photocatalyst was added to 150 mL of an aqueous solution containing 10 mg/L MO. Then, the suspension was stirred for 30 min in the dark to attain adsorption-desorption equilibrium. After that, the suspension was irradiated using a Xe lamp, and 7 mL of the solution was sampled and centrifuged to remove the catalysts at 5 min time intervals. The concentration of MO in the degraded solution was detected by UV-vis spectroscopy at 465 nm.

Results and Discussion

Structure and Morphology Analysis

The XRD patterns of $\text{BiOBr}_{0.3}\text{I}_{0.7}$, BAA- x and $\text{BiOBr}_{0.3}\text{I}_{0.7}/\text{AgI}$ are shown in Fig. 1a. All the diffraction peaks of $\text{BiOBr}_{0.3}\text{I}_{0.7}$ can be found in BAA- x and $\text{BiOBr}_{0.3}\text{I}_{0.7}/\text{AgI}$, which indicates that the construction of the Z-scheme photocatalytic system did not change the crystal phase of $\text{BiOBr}_{0.3}\text{I}_{0.7}$. The diffraction peak around 23.7 degrees belongs to AgI (JCPDS No. 09-0399), corresponding to the (111) diffraction. With an increasing

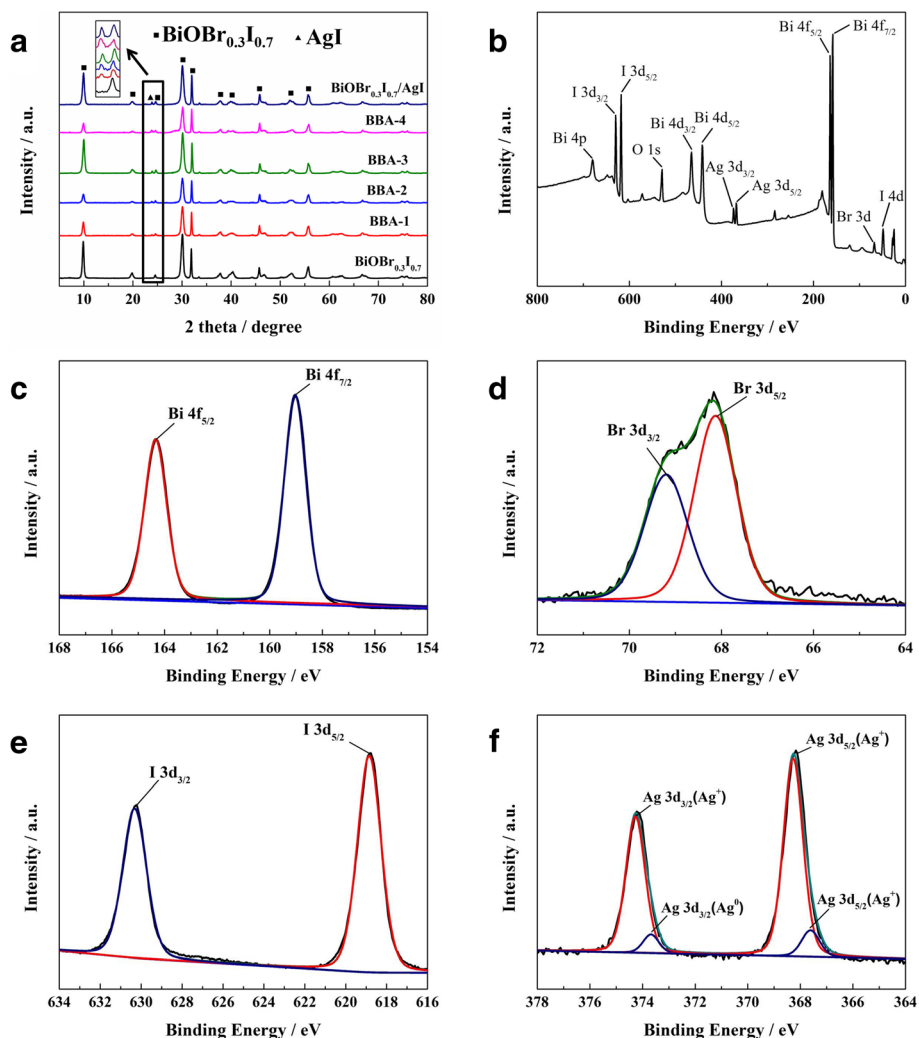


Fig. 1 XRD patterns of $\text{BiOBr}_{0.3}\text{I}_{0.7}$, BAA- x and $\text{BiOBr}_{0.3}\text{I}_{0.7}/\text{AgI}$ (a), XPS survey spectra of BAA-15 (b), BAA-15 XPS spectra of Bi 4f (c), Br 3d (d), I 3d (e), and Ag 3d (f)

elemental Ag ratio, the intensity of the diffraction peak of BAA- x at 23.7 degrees is increased, indicating that the AgI is deposited on the BAA- x surface. In addition, no diffraction peaks for Ag^0 were found, due to its low content.

The morphology and microstructure of the samples were examined by SEM and TEM. The nanoplate structure with a size of 200 to 600 nm is related to $\text{BiOBr}_{0.3}\text{I}_{0.7}$ [13]. It can be observed that the small particle, approximately 10 nm in size, and the plate-like structure were formed in situ on the surface of $\text{BiOBr}_{0.3}\text{I}_{0.7}$, which can be related to Ag and AgI (Fig. 2a). To further investigate the morphology of BAA- x , TEM and HRTEM images were recorded, as well as Fourier transform infrared (FFT) images. It is clear that AgI and Ag nanoparticles were formed in situ on the surface of $\text{BiOBr}_{0.3}\text{I}_{0.7}$, which is in agreement with the SEM result (Fig. 2b). The lattice

of Ag (0.233 nm), AgI (approximately 0.350 nm), and $\text{BiOBr}_{0.3}\text{I}_{0.7}$ (approximately 0.285 nm) can be observed (Fig. 2c), indicating that Ag nanoparticles were formed in situ on the surface of the $\text{BiOBr}_{0.3}\text{I}_{0.7}$, making contact with $\text{BiOBr}_{0.3}\text{I}_{0.7}$ and AgI. Figure 2d shows the structure of $\text{BiOBr}_{0.3}\text{I}_{0.7}/\text{AgI}$ and the junction between $\text{BiOBr}_{0.3}\text{I}_{0.7}$ and AgI; no Ag particle was observed. According to the SEM and TEM results, the BAA- x Z-scheme photocatalyst was successfully synthesized via in situ precipitation and photo-reduction methods.

Composition Analysis and Optical Properties

The chemical composition and chemical state of BAA- x were analyzed by XPS spectroscopy. From the XPS survey spectrum (Fig. 1b), Bi, Br, I, O, and Ag were observed for the BAA- x sample. The strongest peaks at 164 eV and 159 eV correspond to Bi 4f_{5/2} and Bi 4f_{7/2}

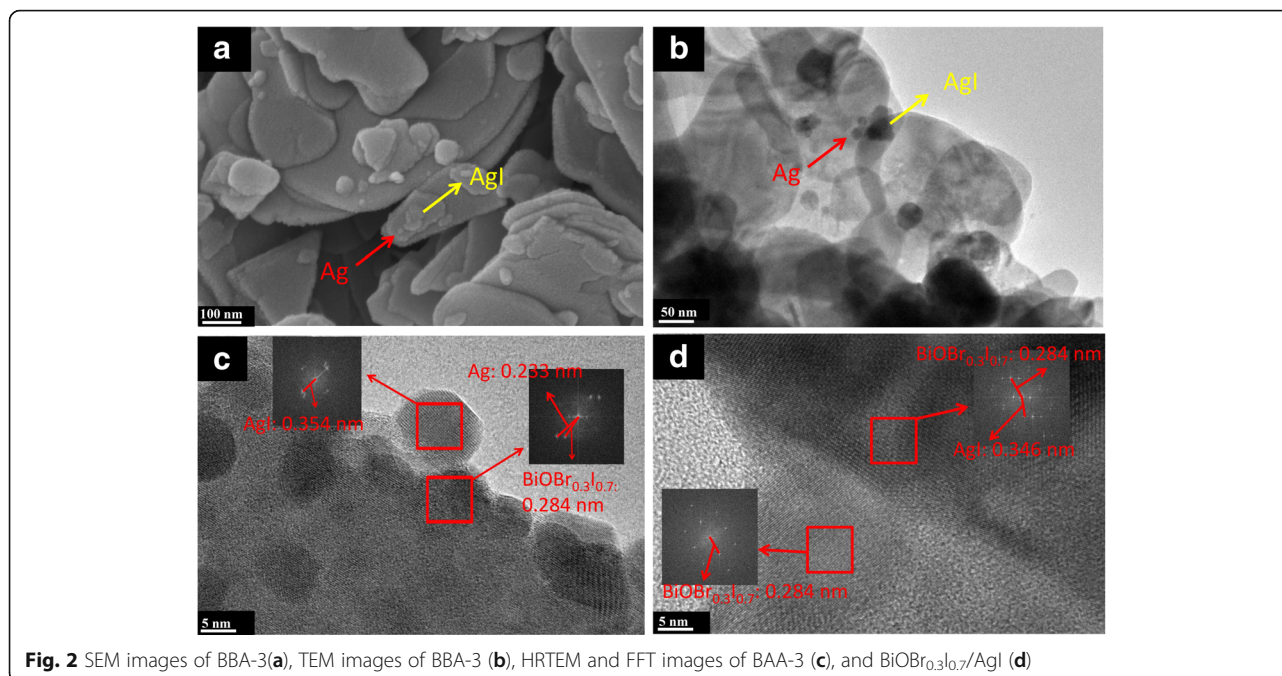


(Fig. 1c). The Br peak can be resolved into two components: the peak at 69 eV belongs to Br $3d_{3/2}$, while the peak at 68 eV belongs to Br $3d_{5/2}$ (Fig. 1d). The I peaks at 630 eV and 619 eV can be attributed to I $3d_{3/2}$ and I $3d_{5/2}$, respectively (Fig. 1e). The Ag 3d peaks can be separated as Ag^+ peaks and Ag^0 peaks. The strong peaks at 374.2 eV and 368.2 eV can be assigned to Ag^+ in BBA- x . The weak peaks at 373.6 eV and 367.6 eV can be assigned to Ag^0 in BBA- x , indicating the existence of metallic Ag nanoparticles on the surface of the BAA- x sample (Fig. 1f).

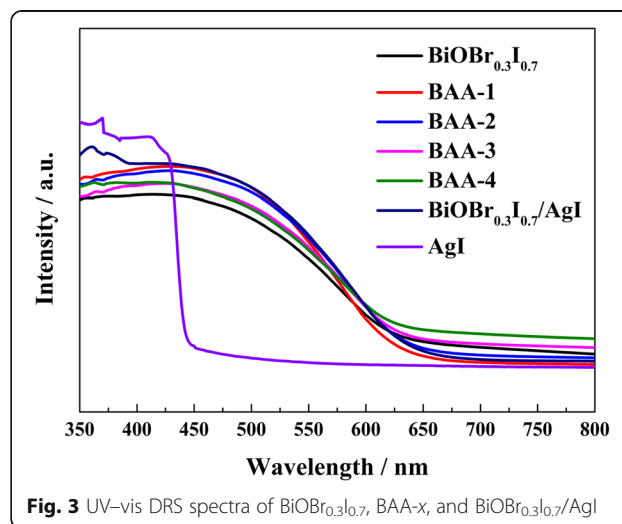
The actual composition of the as-prepared samples was determined by SEM-EDS analysis. As shown in Table 1, the $\text{BiOBr}_{0.3}\text{I}_{0.7}/\text{AgI}$ sample contains approximately 2.79% AgI, and the ratio of the rest of the elemental I to the elemental Br is approximately 7/3, implying that the deposited AgI does not change the element composition of $\text{BiOBr}_{0.3}\text{I}_{0.7}$. After light irradiation, the Ag element content in BAA-3 is higher than that in $\text{BiOBr}_{0.3}\text{I}_{0.7}/\text{AgI}$, indicating that metallic Ag is formed by in situ photo-reduction. The actual AgI and Ag contents of the

Table 1 EDS result of BAA- x samples and $\text{BiOBr}_{0.3}\text{I}_{0.7}/\text{AgI}$

Sample	Atom content (at. %)				AgI (%)	Metallic Ag (%)
	Bi	I	Br	Ag		
BAA-1	49.51	35.23	13.37	1.87	0.573	1.297
BAA-2	47.08	34.62	15.5	2.81	1.664	1.146
BAA-3	47.36	34.37	12.91	5.35	1.218	4.132
BAA-4	46.44	33.47	14.68	5.41	0.962	4.448
$\text{BiOBr}_{0.3}\text{I}_{0.7}/\text{AgI}$	50.75	33.4	13.06	2.79	2.79	0

BAA- x samples were calculated from SEM-EDS data (Table 1). The AgI content in the BAA- x sample was calculated from the Bi element content based on the Bi/I ratio in $\text{BiOBr}_{0.3}\text{I}_{0.7}$. The total Ag element content can be divided into two parts: AgI and metallic Ag; thus, the metallic Ag content can be calculated by the total Ag element content and AgI content. Metallic Ag can be found from all the BAA- x samples, indicating that Ag nanoparticles can be reduced by photo irradiation.

Figure 3 shows the UV–visible diffuse reflectance spectroscopy (DRS) results of the obtained photocatalysts and AgI. AgI has an absorption edge at approximately 450 nm, while $\text{BiOBr}_{0.3}\text{I}_{0.7}$ has a broader absorption in the visible



region from 400 to 650 nm. All BAA-*x* samples have similar absorption regions as BiOBr_{0.3}I_{0.7}, while BAA-*x* exhibits stronger visible light absorption from 400 to 575 nm. As the Ag element content increases in BAA-*x*, the visible light absorption ability slightly decreases. According to previous reports, samples with a surface plasmon resonance (SPR) effect of Ag exhibit a noticeable increasing absorption band in the visible light range [25–27]. However, with the increase in Ag element content, BAA-*x* samples do not show an absorption band that could be assigned to the SPR effect of Ag, indicating that the SPR effect of Ag is insignificant in the BAA-*x* samples [28].

The band gap potential of BiOBr_{0.3}I_{0.7} and AgI was calculated by the Kubelka–Munk method based on the UV–vis DRS spectra, which are 1.61 eV and 2.83 eV for BiOBr_{0.3}I_{0.7} and AgI, respectively. The band structures of BiOBr_{0.3}I_{0.7} and AgI were calculated by the following empirical formulas.

$$E_{VB} = \chi - E_e + 0.5E_g \quad (1)$$

$$E_{CB} = E_v - E_g \quad (2)$$

where E_g is the band gap potential, E_{VB} is the valence band potential, E_{CB} is the conduction band potential, E_e is the energy of free electrons on the hydrogen scale, which is approximately 4.5 eV, and χ is the absolute electronegativity of the semiconductor, expressed as the geometric mean of the absolute electronegativity of the constituent atoms. Thus, the E_{VB} of BiOBr_{0.3}I_{0.7} and AgI were calculated to be 2.71 eV and 2.52 eV vs. normal hydrogen electrode (NHE) and their corresponding E_{CB} are 1.10 eV and –0.31 eV vs. NHE, respectively, which are in agreement with previous reports [13, 21].

Photocatalytic Activity and Mechanism Experiments

The photocatalytic activity of the prepared samples was evaluated by degradation of MO under visible light irradiation. Based on the blank (in the absence of any catalyst) experiment, the self-photolysis of MO under visible light irradiation can be ignored. As shown in Fig. 4, BAA-*x* exhibited superior photocatalytic activity compared with BiOBr_{0.3}I_{0.7} and pure AgI. With the increase in Ag element content, the photocatalytic activity of BAA-*x* increased first and then decreased. This tendency matches with the previous reports of noble metal decorated semiconductors [28–31]. According to the EDS result and photocatalytic activity experiments, with a low added Ag element ratio (5%), the low amount of AgI cannot construct an efficient Z-scheme system to facilitate separation of the photo-generated carrier. When the added Ag element ratio was increased to 15%, BAA-3 exhibited the highest photocatalytic activity among the BAA-*x* photocatalysts, which degraded approximately 89% of MO within 20 min under visible light irradiation. This result indicated that the charge separation is

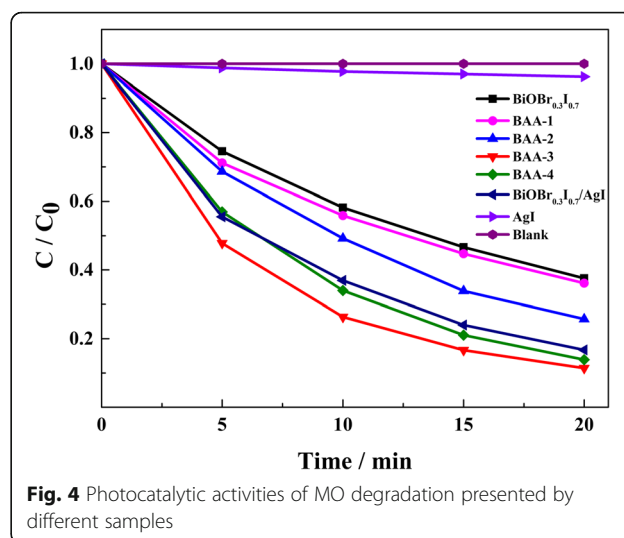
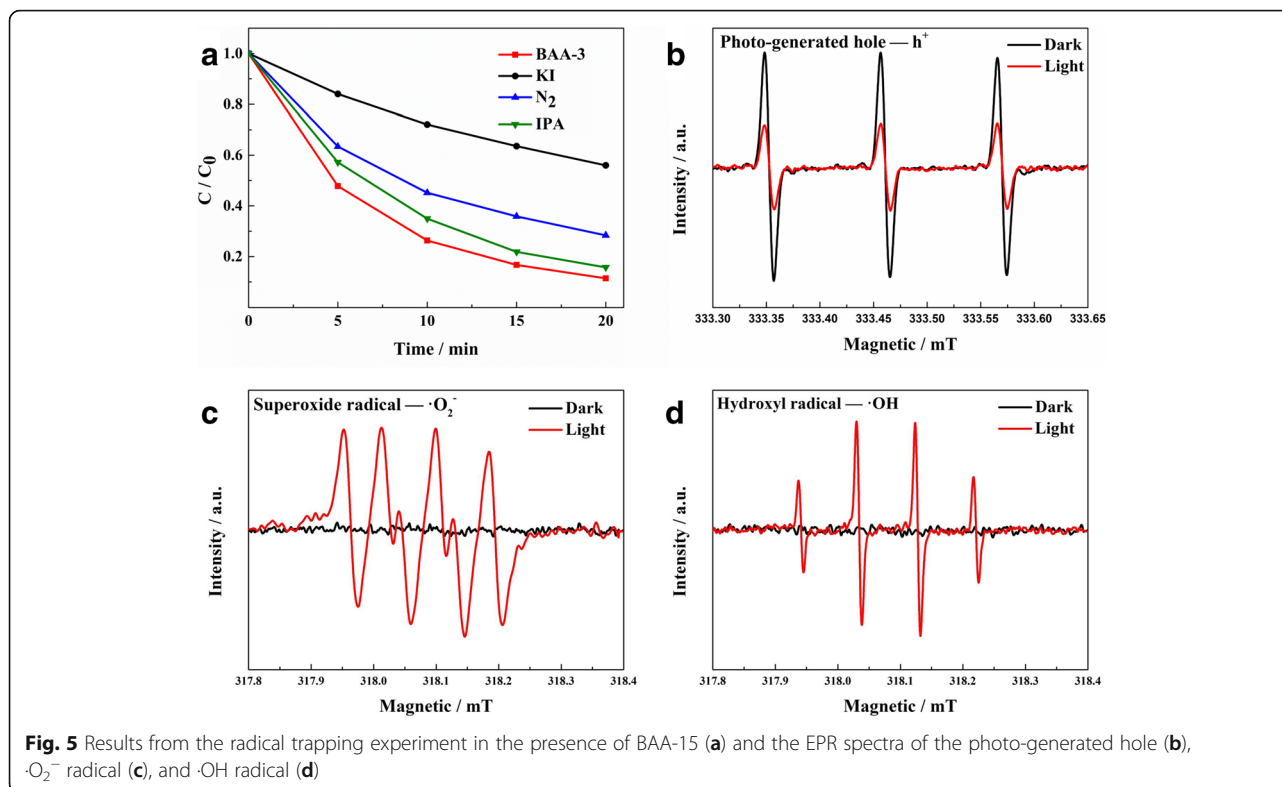


Fig. 4 Photocatalytic activities of MO degradation presented by different samples

more efficient for increased amounts of Ag nanoparticles. After increasing the added Ag element ratio to 20%, the photocatalytic activity of BAA-4 was depressed. The reason may be that the low AgI content led to excess Ag nanoparticles on the surface. Then, the excess Ag nanoparticles may have accumulated electrons, which attracted photo-generated holes, leading to the interfacial electron–hole recombination. BAA-3 exhibits higher photocatalytic activity than BiOBr_{0.3}I_{0.7}/AgI with the same elemental Ag content, demonstrating that the formation of Ag nanoparticles can improve the photocatalytic activity of BAA-*x*. Based on the above discussion, a conclusion can be drawn that BAA-*x* has a higher redox capability than BiOBr_{0.3}I_{0.7}, demonstrating that the fabrication of a Z-scheme photocatalytic system between BiOBr_{0.3}I_{0.7} and AgI is an efficient strategy to improve the photocatalytic activity and the redox capability of BiOBr_{0.3}I_{0.7}.

In order to identify which radical species is the major active species in the photocatalytic process, radical trapping experiments and EPR measurements were carried out to examine the photocatalytic mechanism of BAA-*x*. In the radical trapping experiments, tertiary butanol (t-BuOH), N₂, and potassium iodide (KI) were added as scavengers for hydroxyl radicals ($\cdot\text{OH}$), superoxide radicals ($\cdot\text{O}_2^-$), and holes (h^+), respectively. KI and N₂ have an obvious inhibition effect on the photocatalytic activity of BAA-3 (Fig. 5a), indicating that h^+ and $\cdot\text{O}_2^-$ are the dominant active species, and h^+ is the main active species in photocatalytic degradation. The photocatalytic activity of BAA-3 is slightly inhibited by the addition t-BuOH, indicating that a low amount of $\cdot\text{OH}$ was formed during the photocatalytic process. Meanwhile, from EPR experiments (Fig. 5b–d), when BAA-3 is under visible light irradiation, $\cdot\text{OH}$ and $\cdot\text{O}_2^-$ signals can be detected and the h^+ scavenger 2,2,6,6-tetramethylpiperidine (TEMP) signal is decreased, which is in agreement with the radical trapping experiment. According

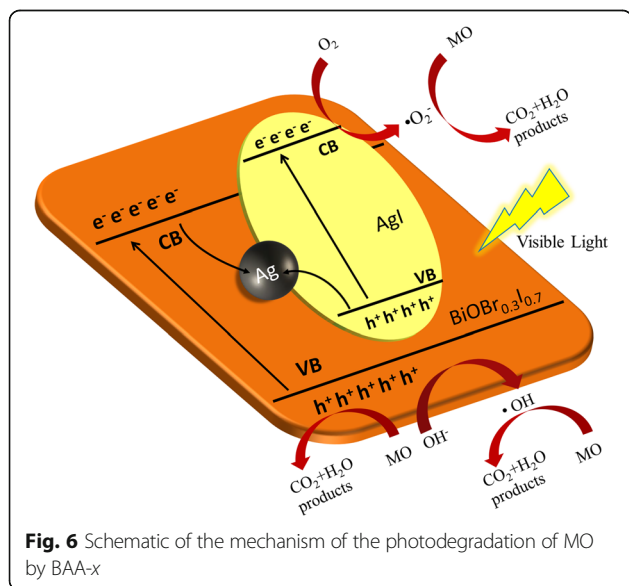


to the mechanism and band structure study, the possible Z-scheme photocatalytic mechanism of BAA-*x* is shown in Fig. 6. Under visible light irradiation, the electrons in the valence band (VB) of $\text{BiOBr}_{0.3}\text{I}_{0.7}$ and AgI are both excited to their conduction band (CB); after that, the photo-generated electrons in the CB bottom of $\text{BiOBr}_{0.3}\text{I}_{0.7}$ move to Ag nanoparticles and then continue to shift to the VB top of AgI, recombining with the photo-generated holes

there. The remaining photo-generated electrons in the CB of AgI (-0.31 eV) with more negative potential exhibit strong reduction ability and react with O_2 ($\text{O}_2/\cdot\text{O}_2^- = -0.046$ eV, vs. NHE) [21], allowing $\cdot\text{O}_2^-$ to degrade MO. Meanwhile, the photo-generated holes (2.71 eV) in the VB of $\text{BiOBr}_{0.3}\text{I}_{0.7}$ display strong oxidation ability to directly degrade MO, and according to the radical trapping experiments, a small number of photo-generated holes react with H_2O to generate $\cdot\text{OH}$ ($\cdot\text{OH}/\text{OH} = 1.99$ eV, vs. NHE) [32], which can further degrade MO.

Conclusion

Novel all-solid-state Z-scheme BAA-*x* photocatalysts were prepared via facile in situ precipitation and photo-reduction methods. BAA-*x* exhibited excellent photocatalytic activity for the degradation of MO compared to $\text{BiOBr}_{0.3}\text{I}_{0.7}$ under visible-light irradiation. Enhancement of the photocatalytic activity is probably related to the special Z-scheme charge-carrier migration pathway, leading to the efficient separation of the photo-generated electron-hole pairs and sustained high redox capability. The optimal added Ag element molar ratio of BAA-*x* is 15%. Mechanistic experiments indicated that $\cdot\text{O}_2^-$ and h^+ are the active radicals and that a low amount of $\cdot\text{OH}$ is generated during photocatalytic degradation. Based on the above study, BAA-*x* shows potential for practical application in environmental purification of organic pollutants.



Abbreviations

AM 1.5: Air mass 1.5; CB: Conduction band; EDS: Energy-dispersive spectroscopy; EPR: Electron paramagnetic resonance; FFT: Fourier transform infrared; HRTEM: High-resolution transmission electron microscopy; MO: Methyl orange; NHE: Normal hydrogen electrode; SEM: Scanning electron microscopy; SPR: Surface plasmon resonance; t-BuOH: Tertiary butanol; TEM: Transmission electron microscopy; UV-Vis DRS: Ultraviolet-visible diffuse reflectance spectroscopy; VB: Valence band; XPS: X-ray photoelectron spectroscopy; XRD: X-ray diffraction

Acknowledgements

The authors acknowledge the financial support from the National Natural Science Foundation of China Program (No. 51602111), the Cultivation Project of the National Engineering Technology Center (2017B090903008), the Xijiang R&D Team (X.W.), a Guangdong Provincial Grant (2015A030310196, 2017A050506009), the Special Fund Project of Science and Technology Application in Guangdong (2017B020240002), and the 111 Project.

Funding

This study was funded by the National Natural Science Foundation of China Program (No. 51602111), the Cultivation Project of the National Engineering Technology Center (2017B090903008), the Xijiang R&D Team (X.W.), a Guangdong Provincial Grant (2015A030310196, 2017A050506009), and the Science and Technology Application in Guangdong (2017B020240002).

Availability of Data and Materials

All data are fully available without restriction.

Authors' Contributions

XW and ZC conceived and designed the experiments. JL and CS performed the experiments. XW, QM, JL, and GZ analyzed the data. XW contributed reagents/materials/analysis tools. The other authors provided assistance with the manuscript writing. All authors read and approved the final manuscript.

Competing Interests

The authors declare that they have no competing interests.

Publisher's Note

Springer Nature remains neutral with regard to jurisdictional claims in published maps and institutional affiliations.

Author details

¹South China Academy of Advanced Optoelectronics, South China Normal University, Guangzhou, Guangdong, Province, China. ²Shenyang Institute of Automation, Chinese Academy of Sciences, Guangzhou 511458, China. ³International Academy of Optoelectronics, South China Normal University, Zhaoqing, Guangdong Province, China. ⁴Institute of Solar Energy, Yunnan Normal University, Kunming 650500, People's Republic of China.

Received: 31 May 2018 Accepted: 28 October 2018

Published online: 20 November 2018

References

- Shimura K, Yoshida H (2010) Heterogeneous photocatalytic hydrogen production from water and biomass derivatives. *Energy Environ Sci* 4:2467
- Li J, Li H, Zhan G, Zhang L (2017) Solar water splitting and nitrogen fixation with layered bismuth oxyhalides. *Acc Chem Res* 50:112–121
- Gao C, Meng Q, Zhao K, Yin H, Wang D, Guo J, Zhao S, Chang L, He M, Li Q, Zhao H, Huang H, Gao Y, Tang Z (2016) Co₃O₄ hexagonal platelets with controllable facets enabling highly efficient visible-light photocatalytic reduction of CO₂. *Adv Mater* 28:6485–6490
- Manzi A, Simon T, Sonleitner C, Doblinger M, Wyrwich R, Stern O, Stolarczyk JK, Feldmann J (2015) Light-induced cation exchange for copper sulfide based CO₂ reduction. *J Am Chem Soc* 137:14007–14010
- Wang X, Wang F, Sang Y, Liu H (2017) Full-spectrum solar-light-activated photocatalysts for light-chemical energy conversion. *Adv Energy Mater* 7: 1700473
- Kuriki R, Yamamoto M, Higuchi K, Yamamoto Y, Akatsuka M, Lu D, Yagi S, Yoshida T, Ishitani O, Maeda K (2017) Robust binding between carbon nitride nanosheets and a binuclear ruthenium(II) complex enabling durable, selective CO₂ reduction under visible light in aqueous solution. *Angew Chem Int Ed Engl* 56:4867–4871
- Fujishima A, Zhang X, Tryk DA (2008) TiO₂ photocatalysis and related surface phenomena. *Surf Sci Rep* 63:515–582
- Chong MN, Jin B, Chow CWK, Saint C (2010) Recent developments in photocatalytic water treatment technology: a review. *Water Res* 44:2997–3027
- Kansal SK, Lamba R, Mehta SK, Umar A (2013) Photocatalytic degradation of Alizarin Red S using simply synthesized ZnO nanoparticles. *Mater Lett* 106: 385–389
- Barrocas B, Entradas TJ, Nunes CD, Monteiro OC (2017) Titanate nanofibers sensitized with ZnS and Ag₂S nanoparticles as novel photocatalysts for phenol removal. *Appl Catal B* 218:709–720
- Tanwar R, Kaur B, Mandal UK (2017) Highly efficient and visible light driven Ni_{0.5}Zn_{0.5}Fe₂O₄@PANI modified BiOCl heterocomposite catalyst for water remediation. *Appl Catal B* 211:305–322
- Ma G, Chen Z, Chen Z, Jin M, Meng Q, Yuan M, Wang X, Liu JM, Zhou G (2017) Constructing novel WO₃/Fe (III) nanofibers photocatalysts with enhanced visible-light-driven photocatalytic activity via interfacial charge transfer effect. *Mater Today Energy* 3:45–52
- Lu J, Meng Q, Lv H, Shui L, Jin M, Zhang Z, Chen Z, Yuan M, Wang X, Liu JM, Zhou G (2018) Synthesis of visible-light-driven BiOBr_xI_{1-x} solid solution nanoplates by ultrasound-assisted hydrolysis method with tunable bandgap and superior photocatalytic activity. *J Alloys Compd* 732:167–177
- Zhang X, Wang CY, Wang LW, Huang GX, Wang WK, Yu HQ (2016) Fabrication of BiOBr_xI_{1-x} photocatalysts with tunable visible light catalytic activity by modulating band structures. *Sci Rep* 6:22800
- Zhou P, Yu J, Jaroniec M (2014) All-solid-state Z-scheme photocatalytic systems. *Adv Mater* 26:4920–4935
- Li H, Tu W, Zhou Y, Zou Z (2016) Z-scheme photocatalytic systems for promoting photocatalytic performance: recent progress and future challenges. *Adv Sci* 3:1500389
- Tateishi I, Katsumata H, Suzuki T, Kaneko S (2017) Z-scheme photocatalytic activity of g-C₃N₄/tetrahedral Ag₃PO₄ hybrids under visible light. *Mater Lett* 201:66–69
- Li JM, Cheng HY, Chiu YH, Hsu YJ (2016) ZnO-Au-SnO₂ Z-scheme photoanodes for remarkable photoelectrochemical water splitting. *Nanoscale* 8:15720–15729
- Pu YC, Lin WH, Hsu YJ (2015) Modulation of charge carrier dynamics of Na_xH_{2-x}Ti₃O₇-Au-Cu₂O Z-scheme nanoheterostructures through size effect. *Appl Catal B* 163:343–351
- Chiu YH, Hsu YJ (2017) Au@Cu₇S₄ yolk@shell nanocrystal-decorated TiO₂ nanowires as an all-day-active photocatalyst for environmental purification. *Nano Energy* 31:286–295
- Chen Z, Wang W, Zhang Z, Fang X (2013) High-efficiency visible-light-driven Ag₃PO₄/AgI photocatalysts: Z-scheme photocatalytic mechanism for their enhanced photocatalytic activity. *J Phys Chem C* 117:19346–19352
- Lin H, Cao J, Luo B, Xu B, Chen S (2012) Synthesis of novel Z-scheme AgI/Ag/AgBr composite with enhanced visible light photocatalytic activity. *Catal Commun* 21:91–95
- Wang Y, Niu C, Zhang L, Wang Y, Zhang H, Huang D, Zhang X, Wang L, Zeng G (2016) High-efficiency visible-light AgI/Ag/Bi₂MoO₆ as a Z-scheme photocatalyst for environmental applications. *RSC Adv* 6:10221–10228
- Liang L, Cao J, Lin H, Zhang M, Guo X, Chen S (2017) A novel double visible light active Z-scheme AgI/AgI-(BiO)₂CO₃ composite: automatic formation of Ag bridge in the photocatalytic process. *Mater Res Bull* 94:291–297
- Wei T, Gao S, Wang Q, Xu H, Wang Z, Huang B, Dai Y (2017) Transformation from Ag@Ag₃PO₄ to Ag@Ag₂SO₄ hybrid at room temperature: preparation and its visible light photocatalytic activity. *J Nanopart Res* 19:34
- Jiang Z, Zhang X, Yuan Z, Chen J, Huang B, Dionysiou DD, Yang G (2018) Enhanced photocatalytic CO₂ reduction via the synergistic effect between Ag and activated carbon in TiO₂/AC-Ag ternary composite. *Chem Eng J* 348:592–598
- Liang X, Wang P, Li M, Zhang Q, Wang Z, Dai Y, Zhang X, Liu Y, Whangbo MH, Huang B (2018) Adsorption of gaseous ethylene via induced polarization on plasmonic photocatalyst Ag/AgCl/TiO₂ and subsequent photodegradation. *Appl Catal B* 220:356–361
- Hsu YH, Nguyen AT, Chiu YH, Li JM, Hsu YJ (2016) Au-decorated GaOOH nanorods enhanced the performance of direct methanol fuel cells under light illumination. *Appl Catal B* 185:133–140
- Chen YC, Pu YC, Hsu YJ (2012) Interfacial charge carrier dynamics of the three-component In₂O₃-TiO₂-Pt heterojunction system. *J Phys Chem C* 116: 2967–2975

30. Lin WH, Chiu YH, Shao PW, Hsu YJ (2016) Metal-particle-decorated ZnO nanocrystals: photocatalysis and charge dynamics. *ACS Appl Mater Interfaces* 8:32754–32763
31. Chiu YH, Chang KD, Hsu YJ (2016) Plasmon-mediated charge dynamics and photoactivity enhancement for Au-decorated ZnO nanocrystals. *J Mater Chem A* 6:4286–4296
32. Shan W, Hu Y, Bai Z, Zheng M, Wei C (2016) In situ preparation of g-C₃N₄/bismuth-based oxide nanocomposites with enhanced photocatalytic activity. *Appl Catal B* 188:1–12

Submit your manuscript to a SpringerOpen[®] journal and benefit from:

- ▶ Convenient online submission
- ▶ Rigorous peer review
- ▶ Open access: articles freely available online
- ▶ High visibility within the field
- ▶ Retaining the copyright to your article

Submit your next manuscript at ▶ [springeropen.com](https://www.springeropen.com)
